Organic matter from the Chicxulub crater exacerbated the K–Pg impact winter

Shelby L. Lyons[a,1], Allison T. Karp[a], Timothy J. Bralower[a], Kliti Grice[b], Bettina Schaefer[b], Sean P. S. Gulick[c,d,e], Joanna V. Morgan[f], and Katherine H. Freeman[a]

[a]Department of Geosciences, The Pennsylvania State University, University Park, PA 16802; [b]Western Australia Organic and Isotope Geochemistry Centre, School of Earth and Planetary Sciences, The Institute for Geoscience Research, Curtin University, Perth, WA 6102, Australia; [c]Institute for Geophysics, University of Texas at Austin, Austin, TX 78758; [d]Department of Geological Sciences, University of Texas at Austin, Austin, TX 78712; [e]Center for Planetary Systems Habitability, University of Texas at Austin, Austin, TX 78712; and [f]Department of Earth Science and Engineering, Imperial College London, London SW7 2AZ, United Kingdom

Edited by Mark Thiemens, University of California San Diego, La Jolla, CA, and approved August 24, 2020 (received for review March 11, 2020)

An asteroid impact in the Yucatán Peninsula set off a sequence of events that led to the Cretaceous–Paleogene (K–Pg) mass extinction of 76% species, including the nonavian dinosaurs. The impact hit a carbonate platform and released sulfate aerosols and dust into Earth's upper atmosphere, which cooled and darkened the planet—a scenario known as an impact winter. Organic burn markers are observed in K–Pg boundary records globally, but their source is debated. If some were derived from sedimentary carbon, and not solely wildfires, it implies soot from the target rock also contributed to the impact winter. Characteristics of polycyclic aromatic hydrocarbons (PAHs) in the Chicxulub crater sediments and at two deep ocean sites indicate a fossil carbon source that experienced rapid heating, consistent with organic matter ejected during the formation of the crater. Furthermore, PAH size distributions proximal and distal to the crater indicate the ejected carbon was dispersed globally by atmospheric processes. Molecular and charcoal evidence indicates wildfires were also present but more delayed and protracted and likely played a less acute role in biotic extinctions than previously suggested. Based on stratigraphy near the crater, between 7.5×10^{14} and 2.5×10^{15} g of black carbon was released from the target and ejected into the atmosphere, where it circulated the globe within a few hours. This carbon, together with sulfate aerosols and dust, initiated an impact winter and global darkening that curtailed photosynthesis and is widely considered to have caused the K–Pg mass extinction.

Chicxulub impact crater | Cretaceous–Paleogene | polycyclic aromatic hydrocarbons | impact winter | wildfires

Sixty-six million years ago, a ∼12-km-diameter asteroid collided with the Yucatán carbonate platform of the southern Gulf of Mexico (1–4), formed the 190- to 210-km-wide, multiring Chicxulub impact crater (5–7), and ultimately resulted in the Cretaceous–Paleogene (K–Pg) mass extinction (8, 9). The target rock was heated, vaporized, and ejected during the impact event. This released sulfate aerosols and dust, and possibly soot, from the impact site, which reduced the amount of solar radiation that reached the Earth's surface and caused global cooling and darkness (10–16). The cessation of photosynthesis resulting from this impact winter is considered to be the major killing mechanism for the mass extinction (9).

Elevated concentrations of iridium (3) and various burn markers (17–19) are observed in K–Pg boundary records globally (18–25), including within sedimentary rocks deposited at the Chicxulub crater site within days to years after the impact (26) (Fig. 1). We use burn marker as a generic term that does not invoke a source and represents all reduced carbon products of high-temperature processes including soot, charcoal, black carbon, polycyclic aromatic hydrocarbons (PAHs), fullerenes, and carbon cenospheres.

The source of burn markers widely observed at K–Pg boundary sites has been debated for over 30 y (23). Wildfires have been invoked to explain diverse molecular and solid burn markers (18, 23, 26, 29), a small stable carbon isotope excursion in plant wax *n*-alkanes and carbonates (−1.4‰ to −1.8‰; refs. 20 and 39), and charred plant material in K–Pg impact deposits (26, 40). The rapid heating, vaporization, and ejection of petrogenic carbon from the target rock have been invoked to explain carbon cenospheres (19), which are pore-containing organic structures, and PAH distributions at multiple locations (14, 28, 29). Attributing all burn markers to the target rock alone would require invoking organic carbon-rich sediments in the target rock (19) and a larger zone of heating and excavation than suggested for the Chicxulub impact (40, 41), while linking them solely to wildfires would imply between 18% (20) and 100% (32) of the terrestrial biosphere burned with soot production enhanced by up to an order of magnitude over modern fires (32). Most assessments of burn markers cannot distinguish between carbon sourced from fires and carbon from impacted rock. For example, anomalously mature vitrinite in sediments (Caravaca, Spain) could indicate either flash heating by fire, or recycled fossil vitrinite (21). Identical isotope signatures of elemental carbon in K–Pg boundary sediments at many sites ($\delta^{13}C = -25.39 \pm 0.30‰$) suggest a globally homogenized source (18, 32), but are also consistent with both terrestrial biomass (39) and fossil marine organic matter. Finally, nondiagnostic patterns or less explicit explanations of the PAH record (*SI Appendix*) can arise because PAHs can be produced by wildfires, the burning of carbon within

Significance

Burn markers are observed in many records of the Cretaceous–Paleogene asteroid impact and mass extinction event. These materials could be derived from wildfires on land or from sedimentary rocks hit by the asteroid. We present a detailed record of molecular burn markers (polycyclic aromatic hydrocarbons [PAHs]) from the Chicxulub crater and in ocean sediments distant from the impact site. PAH features indicate rapid heating and a fossil carbon source and are consistent with sedimentary carbon ejected from the impact crater and dispersed by the atmosphere. Target rock-derived soot immediately contributed to global cooling and darkening that curtailed photosynthesis and caused widespread extinction. PAH evidence indicates wildfires were present but less influential on global climate and extinction.

Author contributions: S.L.L., T.J.B., S.P.S.G., J.V.M., and K.H.F. designed research; S.L.L., J.V.M., and K.H.F. performed research; S.L.L. contributed new reagents/analytic tools; S.L.L., A.T.K., K.G., B.S., J.V.M., and K.H.F. analyzed data; and S.L.L., A.T.K., T.J.B., K.G., B.S., S.P.S.G., J.V.M., and K.H.F. wrote the paper.

The authors declare no competing interest.

This article is a PNAS Direct Submission.

[1]To whom correspondence may be addressed. Email: shelby.l.lyons@gmail.com.

This article contains supporting information online at https://www.pnas.org/lookup/suppl/doi:10.1073/pnas.2004596117/-/DCSupplemental.

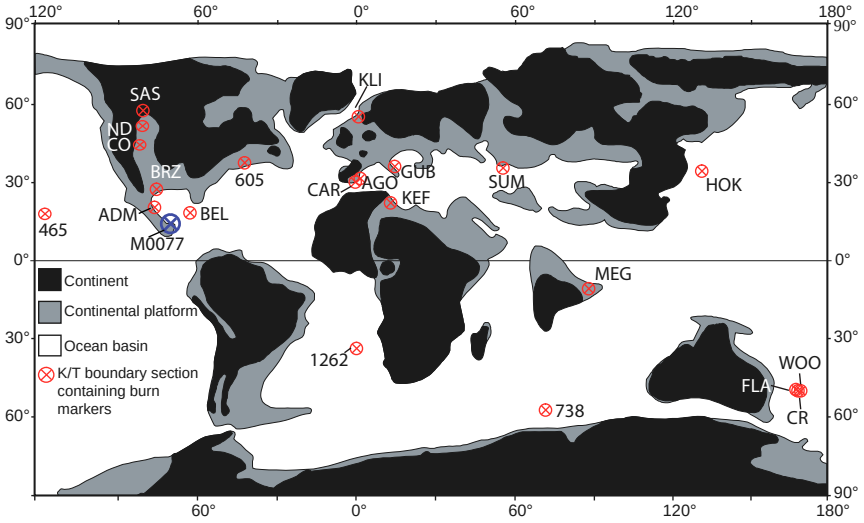

Fig. 1. Compilation of global sites with burn marker observations at the K–Pg boundary. All sites marked in red contain burn markers, including the Chicxulub impact site, marked by a blue cross. Numbers refer to Deep Sea Drilling Project/ODP/IODP sites. ADM, Arroyo de Mimbral, Mexico; AGO, Agost, Spain; BEL, Beloc, Haiti; BRZ, Brazos, Texas, United States; CAR, Caravaca, Spain; CO, Colorado, United States (Madrid East South, Clear Creek North, and Berwind Canyon); CR, Chancet Rocks, New Zealand; FLA, Flaxbourne River, New Zealand; GUB, Gubbio, Italy; HOK, Kawaruppu, Hokkaido, Japan; KEF, El Kef, Tunisia; KLI, Stevns Klint, Denmark; MEG, Meghalaya, India; ND, Mud Buttes, North Dakota, United States; SAS, Saskatchewan, Canada sites (Rock Creek East, Wood Mountain Creek); SUM, Sumbar, Turkmenistan; WOO, Woodside Creek, New Zealand. Sites with elevated total or specific PAH spike: M0077 (26), 738, 1262, MEG (27), CAR (20), KLI (22), GUB (22), WOO (22), HOK (28), ADM (21), ND (29), CO (29), BEL (14), 605 (30). Sites with elevated soot or charcoal: M0077 (26, 31), 738 (31), 1262 (31), CAR (20), KLI (18, 23, 32), GUB (18), WOO (18, 23, 33), ADM (21), CR (18, 33), BRZ (34), KEF (35), AGO (32, 35), SUM (24), 465 (36), SAS (37). Sites with carbon cenospheres: KLI (19), WOO (19), SAS (19). Sites with fullerenes: WOO (38), FLA (38), BRZ (34). Figure modified from Bralower et al. (2020) (31).

the target rock, geological heating and thermal maturation (42), diagenesis (43), fungi (44), and hydrothermal activity (44–47).

The origin of K–Pg burn markers, whether from wildfires or target rock carbon, directly affects our understanding of the consequences of the impact, as soot in the stratosphere acts as a light-absorbing aerosol (14, 16, 48). The anti-greenhouse effects of soot in the upper atmosphere are argued to be a main contributor to the Chicxulub impact winter (14, 16, 48). The excavation and heating of hydrocarbons in the target rock upon impact (14, 19, 29, 37, 49, 50) would have rapidly led to a diverse set of molecular burn markers and debris that were quickly transported away from the impact site. Recent simulations demonstrate that interactions between Chicxulub ejecta and the Earth's atmosphere led to the generation of a fast-moving dust cloud that traveled above the stratosphere and circled the globe within a few hours of the impact (15); this material gradually settled into the stratosphere under Earth's gravity (15). Target-rock–derived soot emplaced in this dust cloud could have persisted in the stratosphere for years (48, 51) until it was likely photochemically removed (14, 51, 52). In contrast, wildfires were ignited immediately by thermal radiation from the impact plume and reentering ejecta in proximal locations, but radiating ejecta could not have ignited flora instantaneously everywhere around the globe (25, 41, 53, 54), as previously suggested (32). If widespread global wildfires are tied to black carbon observed in K–Pg boundary deposits (23, 24, 35), they must have been ignited by natural causes in many regions and over an extended period after the impact (12, 41, 53, 54). Carbon in smoke and aerosols from wildfires is rapidly removed from the lower troposphere via precipitation (14, 51, 52, 55), although some soot can be lofted upward into the stratosphere through solar heating in the months following its generation (48, 51).

Here, we examine PAH burn markers from the impact crater (site M0077) and two distal, deep-ocean locations (sites 738 and 1262) through the lens of physical and environmental chemistry. We use PAH isomer ring configurations to definitively distinguish burned from unburned carbon (regardless of source), and PAH alkylation patterns to distinguish burned biomass from burned petrogenic carbon. For all boundary samples, isomer ring configurations indicate rapid heating, while alkylation patterns indicate a fossil carbon source. Molecular size distributions are consistent with atmospheric transport of carbon from the crater and its subsequent deposition in proximal (site M0077) and distal (sites 738 and 1262) sediments.

The presence of significant quantities of rapidly heated, thermally mature carbon within K–Pg boundary layers is consistent with the release of organic carbon from the target rock and indicates that wildfires were not the only source of burn markers at the event horizon. Burned sedimentary organic carbon released from the excavated carbonate platform traveled around the globe within hours after the impact. While wildfires likely occurred in response to the impact, models and burn marker evidence suggest instead that terrigenous ecosystem destruction via wildfires and placement of wildfire soot in the stratosphere occurred over an extended time period, ultimately delaying its climatic impact. Burning of sedimentary organic carbon in the target rock would have immediately and effectively contributed to impact winter conditions of global cooling and global darkness (14, 15, 29) and resulted in an abrupt reduction in photosynthesis; these are considered the major drivers of the end-Cretaceous mass extinction (9).

Elevated PAH Concentrations at the K–Pg Boundary at Sites M0077, 738, and 1262. PAH concentrations are elevated within the K–Pg boundary intervals at sites M0077, 738, and 1262. Site M0077 (Fig. 1) is the most complete marine record of the immediate postimpact interval (26, 56) and is particularly important due to its completeness and expansion (26), constraints on timing (26, 56, 57), and proximity to the impact itself. The 75-cm-thick micritic limestone ("transitional unit" unit 1G, 616.58 to 617.33 m below sea floor [mbsf]) (26) at site M0077 provides a record of immediate and proximal sources of burn markers, as it was deposited

over months to years following the impact (57) by seiche waves and subsequent settling within the crater (26).

The 3-cm green marlstone capping the transitional unit at site M0077 (616.55 to 616.58 mbsf) and the boundary intervals at Ocean Drilling Program (ODP) site 738 (Kerguelen Plateau, Indian Ocean) (377.04 to 377.16 mbsf) (31, 58, 59) and ODP site 1262 (Walvis Ridge, South Atlantic Ocean) (195.54 mbsf) (31, 60–63) contain airfall-derived input and the extraterrestrial platinum group element anomalies deposited within years following the impact (26, 56, 59, 63, 64) (see *SI Appendix*, Figs. S1–S3 for further discussion). Airfall-derived burn markers at sites 738 and 1262 and within the green marlstone at site M0077 record sustained, globally dispersed burn markers mixed with delayed, regional-scale wildfire responses.

Concentrations of PAHs peak within the K–Pg boundary intervals at all three sites (Fig. 2). Site M0077 has elevated PAH concentrations through the entire 75-cm transitional unit, including samples coeval with charcoal (26), which is most likely derived from terrigenous biomass burning. A local maximum in PAH concentrations within the airfall-derived green marlstone (616.58 to 616.55 mbsf) was coeval with the iridium anomaly (57) and possible airfall-derived charcoal (31). Within centimeters of the K–Pg boundary, total parent PAH concentrations increased by 43 times at site M0077, 9 times at site 738, and 138 times at site 1262 relative to Paleogene sediments, which were used as a comparison due to the lack of Cretaceous rocks preserved at the Chicxulub peak-ring site. The PAH peak abundance at site 738 is offset 9 cm above the boundary clay, within a laminated interval, and coincident with elevated but declining iridium content (65). We suggest this displacement from the boundary resulted from winnowing and redeposition of sediments, which can potentially mix PAHs up-section. At site 1262, the PAH abundance peak is offset 5 cm below the boundary, overlapping with the base of the osmium isotope anomaly (63), which we attribute to downward transport of particles (66) in this heavily bioturbated section (62).

The uncertainty associated with centimeter-scale offsets of PAH peak abundances and other markers for the boundary at sites 738 and 1262 can represent thousands of years. The offsets are larger in magnitude but in the same direction as offsets in the iridium and osmium anomalies at both sites, as well as in other records (14, 20, 28). The depositional offset in PAH records likely reflects transport processes that changed depositional timing, including sorption and ballasting of compounds to minerals and particulate carbon, or postdepositional mobilization via fluid solubilization and migration. Elevated PAH concentrations within centimeters of the K–Pg boundary are also found in Denmark, Italy, New Zealand (22), Spain (20), México (21), Canada, the United States (29), India (27), Haiti (14), Japan (28), and mid-Atlantic Deep Sea Drilling Project site 605 (30). The global occurrence of peaks in PAH concentration at the K–Pg boundary in diverse depositional environments indicates that they are associated directly or indirectly with the impact or its effects.

PAH Characteristics Indicate Rapid Heating of Organic Matter. PAH alkylation, shapes, and sizes can indicate fuel source, heating process, degradation, and transport-related alteration (43). Heating processes that yield PAHs can range from over millions of years at low temperatures (<150 °C), such as during the generation of petroleum (petrogenic), or within seconds at high temperatures (>300 °C, up to 1,000s °C) (43, 68), such as during combustion or pyrolysis. Slow heating in geologic basins or by hydrothermal waters will preferentially generate thermodynamically stable ring configurations. In contrast, rapid condensation of structures at elevated temperatures, as happens during wildfires (43), petroleum burning (68, 69), or by shock heating (70), tend to produce less stable and kinetically favored ring configurations (43). Isomer stability is represented by ratios of benz[*a*]anthracene/(benz[*a*]anthracene + chrysene), fluoranthene/(fluoranthene + pyrene), indeno[1,2,3-cd]pyrene/(indeno[1,2,3-cd]pyrene + benzo[*ghi*]perylene), and anthracene/(anthracene + phenanthrene). The numerator is always the kinetically favored isomer and indices will increase with greater input of PAHs from high-temperature processes. Source cutoffs presented in Fig. 3 are based on the environmental literature (71, 72).

Fast-formed isomers dominate PAHs produced today via combustion or pyrolysis, regardless of fuel source, whereas the more stable isomers dominate PAHs from unburned fossil carbon inputs, including coal, oil, kerogen, and other petrogenic sources (43, 71–74). On geological timescales, thermal maturation of fire-derived organic matter favors thermodynamic isomers that eventually overprint the abundance of kinetic isomers. Similarly, burning of fossil carbon will overprint the thermodynamic forms with newly generated kinetic isomers (68, 69).

At sites M0077 (Fig. 3), 738 (*SI Appendix*, Fig. S7), and 1262 (*SI Appendix*, Fig. S9), PAHs at and surrounding the boundary were consistently dominated by kinetically favored forms as indicated by ratios of isomer pairs (Fig. 3). All isomer pairs indicate a fast, high-temperature formation process. Based on the clear dominance of kinetic isomers, we conclude that K–Pg boundary PAHs at all sites were produced via fast, high-temperature processes,

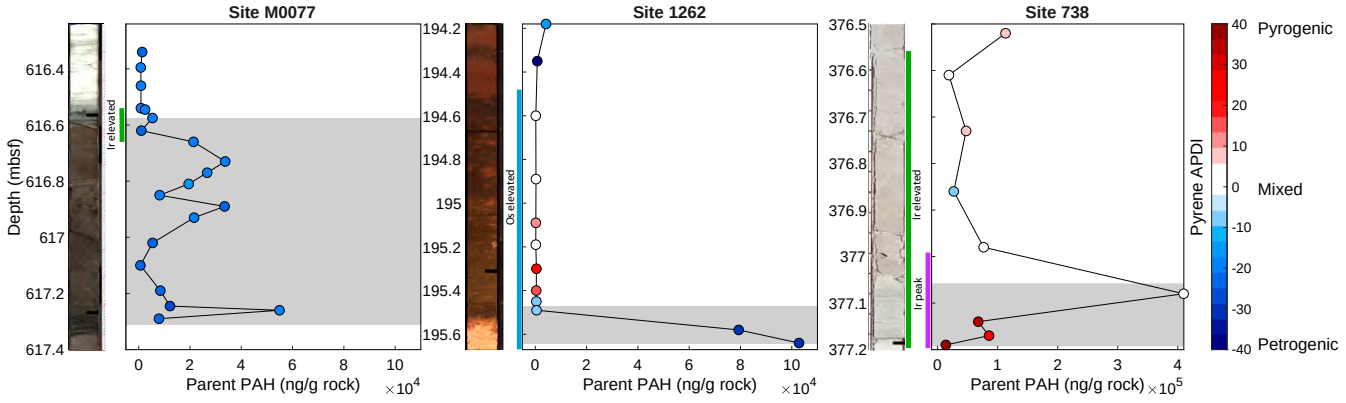

Fig. 2. Parent PAH concentrations across the K–Pg boundary interval for sites M0077, 1262, and 738. K–Pg boundary deposits are highlighted in gray, and samples are colored by the pyrene APDI index (67). Warm colors represent more pyrogenic inputs, cool colors represent more petrogenic inputs, and white represents mixed inputs. Black rectangles on core photographs denote intervals with charcoal observations (26, 31). Vertical green bars represent intervals with elevated (>0.25 ppb) Ir concentrations, and purple bars represent intervals with peak (>1 ppb) Ir concentrations. Vertical blue bars represent intervals with low, extraterrestrial $^{187}Os/^{188}Os$ ratios (57, 59, 63). Sites M0077 and 1262 are displayed on a 0 to 1.1×10^5 ng/g axis; site 738 is displayed on a 0 to 4×10^5 ng/g axis.

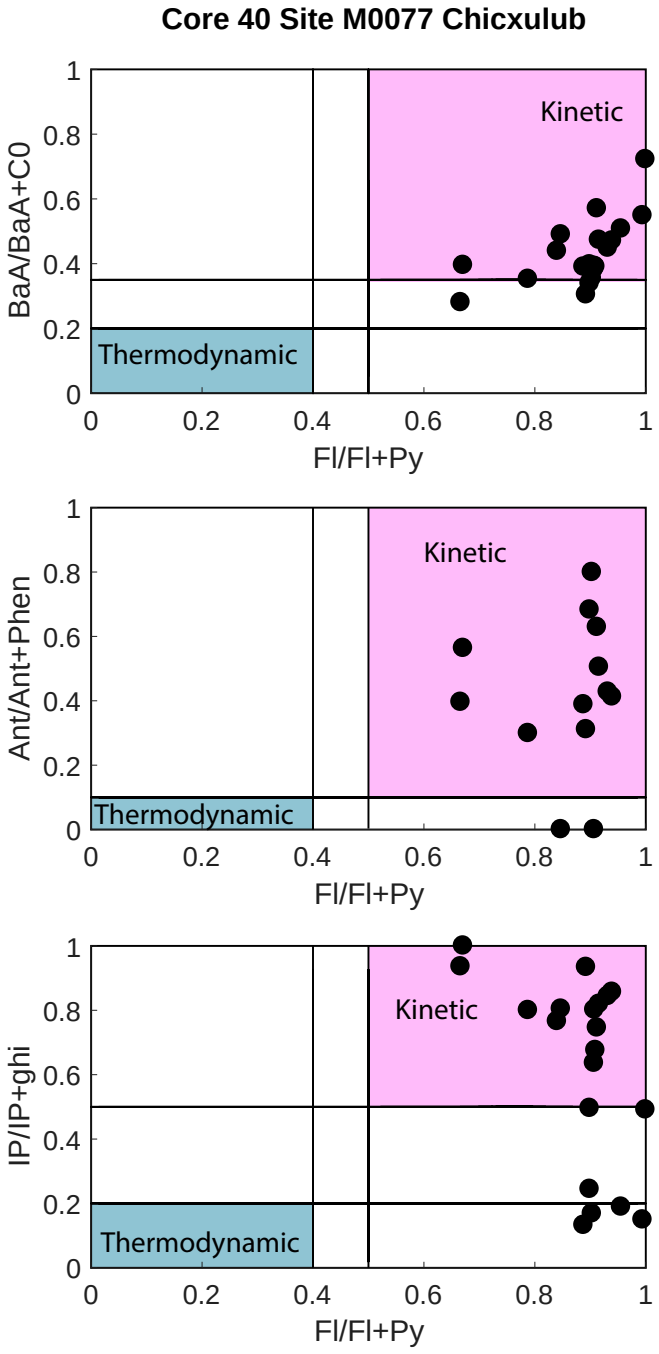

Fig. 3. Chicxulub PAHs ratios are dominated by kinetic isomers based on kinetic/(kinetic + thermodynamic) isomer ratio biplots. Pink quadrants represent kinetically favored PAH ratios, blue quadrants represent thermodynamically favored PAH ratios, and white space indicates mixed kinetic and thermodynamic sources. Solid black lines represent observational cutoff values from Rocha and Palma (71): Fl/Fl+Py: thermodynamic <0.4, kinetic >0.5; BaA/BaA+C0: thermodynamic <0.2, kinetic >0.35; Ant/Ant+Phen: thermodynamic <0.1, kinetic >0.1; IP/IP+ghi: thermodynamic <0.2, kinetic >0.5. PAH abbreviations: Ant, anthracene; BaA, benz[*a*]anthrance; C0, chrysene; Fl, fluoranthene; ghi, benzo[*ghi*]perylene; IP, indeno[1,2,3-c,d]pyrene; Phen, phenanthrene; Py, pyrene (43).

consistent with wildfires, heating and ejection of reduced carbon in the target rock, or both. Critically, these data do not support a meteoritic source (75, 76), unaltered petrogenic source (43), hydrothermal-alteration derived PAHs (46), or the thermal maturation of a fire record, as these processes all favor thermodynamic isomers.

PAH Alkylation Indicates a Petrogenic Fuel Source. Abundance patterns of PAH parent (nonalkylated) and alkylated (1–4 methyl groups) forms distinguish biomass and thermally mature fuel sources. The source-specific alkylation pattern of burned organic matter is preserved at high temperatures, even though ring configurations can be overprinted with kinetic forms (68, 69). Fossil carbon (petrogenic material) is characterized by a greater proportion of alkylated PAH homologs, while combusted biomass products (pyrogenic material) are dominated by parent forms and less alkylated PAHs (43). The extent of alkylation is quantified by the alkylated PAH derivative index (APDI) (67). APDI is a numerical value equal to the difference between the second and first derivative of the quadratic fit to the 0–3 methylation pattern for a given parent structure. Petrogenic PAHs have negative APDI values (less than −10), while pyrogenic samples express positive APDI values (>10), and mixed source samples have values close to 0. While weathering can affect alkylated homolog distributions through the loss of parent PAHs (71, 77), it is possible to distinguish the underlying pyrogenic and petrogenic distributions using the APDI (67).

At site M0077, pyrene APDI values averaged −20.9 ± 2.5 (mean ± σ) within the K–Pg boundary interval, which demonstrates alkylated PAHs came from a fossil carbon source. Consistent with this, bulk organic matter in Chicxulub transitional unit samples is thermally mature, as evidenced by a low hydrogen index (*SI Appendix*, Fig. S50). The petrogenic alkylation patterns and kinetic isomer dominance together indicate the PAH fingerprints at Chicxulub represent rapid alteration of petrogenic organic matter. At site 1262, pyrene APDI values at the elevated PAH interval averaged −28.0 ± 3.6, which indicates alkylated PAHs came from a fossil carbon source. In overlying Paleocene samples at site 1262, PAHs were less concentrated and were mixed (Fig. 2) (APDI = −1.3 ± 17.8) with material sourced from background or impact-induced wildfire regimes. At site 738, a positive but low value for the pyrene APDI (+4.1) at the PAH concentration spike indicates a mixture of burned biomass and fossil carbon. Below the K–Pg boundary, PAH concentrations were an order of magnitude lower and had a pyrene APDI value of +36.1 ± 9.0, a highly pyrogenic signal. The switch from this strongly pyrogenic source to a mixed signature was coincident with increased PAH concentrations and likely represents petrogenic material delivered to the Indian Ocean was superimposed on inputs from a preexisting and persistent fire regime documented on the nearest landmass prior to, and possibly through, the K–Pg boundary (27).

K–Pg boundary PAHs are composed of kinetically favored isomers and petrogenic alkylation patterns at sites M0077, 738, and 1262. These results support the hypothesis that thermally mature organic carbon within the target rock was a significant source for PAHs at the K–Pg boundary. Target rock organics at Chicxulub were pyrolyzed and vaporized on impact, at temperatures that exceeded 1,400 °C (78). The PAHs were redeposited at the impact site as well as globally in ocean sediments containing fallout. The presence of charcoal and molecular markers indicate that wildfires also contributed burn markers to K–Pg boundary sediments (26, 31, 64).

Transport Modified PAH Size Distributions at the Impact and Distal Sites. PAHs can be transported in the atmosphere as gases, aerosols, and associated with smoke or dust particles. PAHs range from small, two- to three-ringed structures to large molecules with six or more rings. Larger PAHs are less volatile than smaller structures and have much lower aqueous solubility, which elevates their affinity for organic carbon (i.e., higher octanol–water partition coefficients, log K_{ow}) (Dataset S5). Larger PAHs are therefore

less susceptible to atmospheric and aqueous transport and are more likely to be sorbed to organic particles and grain coatings.

Transport distance, timing, and delivery mechanism (oceanographic or atmospheric processes) likely affected the size distribution of PAH compounds due to their wide range of aqueous solubility and volatility. We tested the hypothesis that physical and chemical properties account for the molecular size distributions observed at the proximal and distal sites. Multivariate statistical analyses (nonmetric multidimensional scaling [NMDS]) conducted on PAH compositions at sites M0077, 738, and 1262 clearly separated Chicxulub samples from the two distal sites (Fig. 4*A*). Larger, less volatile, and less water-soluble PAHs and samples from site M0077 loaded negatively on NMDS1, while smaller, more volatile, and more soluble PAHs and samples from sites 738 and 1262 loaded positively on NMDS1. This result demonstrates clear molecular size differences between sites that are consistent with transport propensity inferred from compound properties, especially volatility and solubility (Fig. 4 *B* and *C* and *SI Appendix*, Figs. S35–S46).

Transport properties can be proxied by the transport efficiency ratio [TER = (phenanthrene + anthracene + fluoranthrene + pyrene)/(phenanthrene + anthracene + fluoranthene + pyrene + chrysene + benz[*a*]anthracene + benzo[*b*]fluoranthene + benzo[*k*]fluoranthene + benzo[*e*]pyrene + benzo[*a*]pyrene + indeno [1,2,3-cd]pyrene + benzo[*ghi*]perylene)] (67). Low TER values (0.4 to 0.7) indicate abundant larger PAHs that are more difficult to transport, such as those associated with modern char and burn residues. High values (0.8 to 1.0) represent smaller forms, which are more readily partitioned into smoke in modern burns and therefore can be transported longer distances by atmospheric processes (67). The Chicxulub crater site M0077 has low TER values of 0.18 ± 0.12, while the distal sites, 738 and 1262, also have low TER values of 0.68 ± 0.14 and 0.59 ± 0.14, respectively (Fig. 4*B*). The prominence of larger molecules highlighted by low-skewed TER values may reflect the high temperatures of impact processes or, less likely, extensive biodegradation that enhanced the proportion of larger compounds. Although biodegradation can contribute to the dominance of larger PAHs, there is no clear signature for extensive loss of more susceptible biomarkers (79). Furthermore, biodegradation was potentially a factor at all sites, and it cannot alone account for molecular-size differences between sites (*SI Appendix*, Figs. S45 and S46).

Potentially, the smaller size distributions at the distal sites reflect PAHs that were heated to very high temperatures before being ejected from the crater at high velocities, compared to the larger compounds close to the crater (80). We note that at site M0077, locally derived impact material, along with proximal ejecta transported back into the crater via resurge, tsunami, and seiches (26), contributed to the transitional unit. In contrast, high-velocity ejecta delivered to the upper atmosphere (81) would have been globally dispersed prior to fallout. Site M0077 contains elevated concentrations of the least volatile compounds throughout the entire transitional unit. In contrast, smaller PAHs at distal sites 738 and 1262 suggest a relatively well-mixed, volatilely transported source that excluded larger PAH structures. The secondary PAH concentration peak in the green marlstone unit at site M0077 corresponds to components delivered via airfall (26, 31). We suggest PAHs at both distal sites and in the green marlstone represent carbon ejected at high velocity from the impact site that circulated the Earth within the dust cloud (15) and was deposited via sorption or association to dust or soot, fallout, and subsequent marine sedimentation.

The source and formation processes of PAHs are reflected in their composition at the K–Pg boundary at three sites separated by many thousands of kilometers. The molecular data are consistent with the Chicxulub target rock as a major point source of PAH burn markers across the K–Pg boundary, which led to the deposition of larger, less volatile PAHs within the crater, and smaller, more volatile PAHs in the fallout layer around the globe. PAHs both near and distal to the crater were likely heated to high temperatures upon impact prior to ejection from the crater (25) and potentially within the resulting dust cloud (15).

Multiple Sources of Burn Markers at the K–Pg Boundary. It is difficult for mass balance calculations to prove or disprove a specific origin of PAHs due to the possibility of multiple sources of burn markers and the large uncertainty surrounding carbon flux predictions. Furthermore, mass balance-based estimates for each source require assumptions about crustal organic richness, abundance of biomass and plant litter, and burning efficiency (19, 20, 32, 40), and often fall within an order of magnitude of each other. Previous workers have suggested various and overlapping amounts of organics were required to explain each source for global K–Pg burn marker signals. Harvey et al. (19) suggested 10^{16} to 10^{17} g of carbon would have needed to burn with a production efficiency of 0.003% to explain the global abundance of carbon cenospheres (19). Gilmour et al. (32) suggested 10^{18} g C in biomass burned at conditions primed for elevated soot production in order to account for global soot records. Arinobu et al. (20) concluded that 10^{17} g C in biomass burned in order to explain the PAH anomaly.

The Late Cretaceous terrigenous biosphere contained ~1 to 2×10^{18} g C (39). At the 100-km diameter crater, the amount of carbon ejected from the upper 10 to 12 km (~3 km of sedimentary rocks above granitoid basement) was 7.9×10^{16} to $\geq 1.35 \times 10^{17}$ g (48) based on Cretaceous Yucatán stratigraphy (48, 82). Unfortunately, the crater's exact preimpact sedimentary sequences have been lost, and their organic abundances are unknown (81, 83). We also lack robust assessments of the carbon inventory for the terrigenous biosphere in the preimpact world. Furthermore, the mass difference between these two reservoirs alone cannot be used to determine the source or impact of burn markers because we cannot tightly constrain the concentration of carbon within the target rock, the amount of biomass burned, the burn product production rates, or the burning efficiencies and conditions of either. We suggest both biosphere and fossil pools of carbon in the target region could have provided large stocks of fuel to burn upon impact.

Additionally, conflicting interpretations of the source and amount of fuel are to be expected for different burn markers, as their relative production rates vary widely with the source, temperatures, and timescales of target rock and biomass burning (see *SI Appendix* for additional discussion). For example, carbon cenospheres were likely produced via target rock carbon burning (19), charcoal was likely produced from wildfires, whereas PAHs, soot, and fullerenes could have derived from both sources. An understanding of the complexity estimating inputs from biomass via wildfires and petrogenic carbon helps reconcile contrasting interpretations of the geochemical and sedimentary record of burn markers.

Acknowledging these uncertainties, we estimate the mass of black carbon released and burned from the sedimentary target rock at sufficient velocity to circle the Earth and contribute to the impact winter (i.e., ref. 15). Sedimentary material ejected at low velocities was deposited close to the crater, whereas material ejected at >1 km/s was susceptible to emplacement within the dust cloud that traveled around the globe within hours of impact (15). Assuming an impact angle of 60° (84) and a total organic carbon content of 0.24% for the sedimentary rocks at the impact site (48), ejecta simulations (1) suggest the initial (preimpact) mass of organic matter ejected at velocities >1 km/s was ~5×10^{16} g C. Roughly half of this material was heated above 433 K (~2.5×10^{15} g) (15) and became soot, provided oxygen was sufficient for combustion. Currently, there are no data for large impacts that would allow us to determine the proportion of the ejected mass that would be burned or the production rates of various burn markers. Using high temperature and pressure nuclear

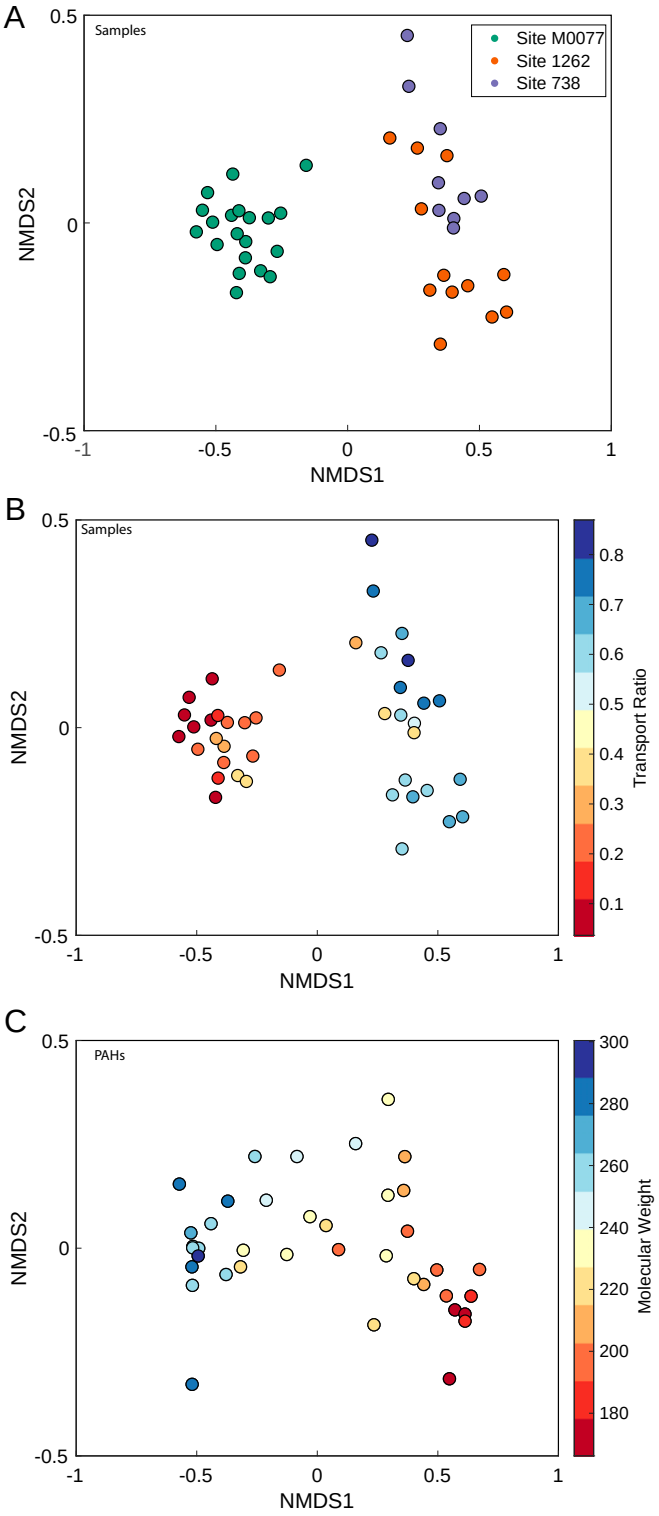

Fig. 4. NMDS of samples from sites M0077, 738, and 1262 demonstrate the effect of transport on PAH composition. (*A*) Samples from all sites plotted based on their NMDS scores colored by location demonstrates a difference in molecular composition between the impact site (site M0077) and the two distal sites (sites 738 and 1262). (*B*) Samples from all sites colored by their transport ratio (67). Low transport ratio values (warm colors) load negatively on NMDS1 and represent PAH compositions difficult to transport; high transport ratio values (cool colors) load positively on NMDS1 and represent PAH compositions more susceptible to transport. (*C*) PAHs plotted by NMDS scores colored by molecular weight. Low-molecular-weight PAHs (warm colors) load positively on NMDS1; high-molecular-weight PAHs (cool colors) load negatively on NMDS1.

warfare soot emission factors of 3 to 10% (84), we estimate between 7.5×10^{14} and 2.5×10^{15} g C of climate-active soot was generated by the impact.

Wolbach et al. (24) estimated 1.5 to 2.0 $\times$ 10^{16} g of fine, climate-active soot in the global K–Pg boundary layer. We suggest that up to 17% (i.e., 2.5×10^{15} g) of this climate-active soot was derived directly from the target rock, while the remainder was sourced from delayed wildfires. Two independent climate simulations show that 5×10^{14} g of soot in the Earth's atmosphere produced significant cooling and darkening, and 1.5×10^{15} g of soot decreased sunlight by 80 to 85% and led to a cooling of 10 to 16 °C (14). These models indicate soot released from the impact site, along with sulfate aerosols and dust (16), initiated global cooling and global darkening, resulting in the loss of photosynthesis considered the likely cause for the K–Pg mass extinction. Wildfires also occurred and destroyed habitats on land in the months following the Chicxulub impact. Wildfire soot, however, was less effectively distributed around the Earth, indicating that its role in the impact winter was delayed. Soot from the target rock, along with sulfate aerosols and dust, initiated the impact winter, while soot released from wildfires potentially increased its severity and extended its duration. The release of molecular burn markers from the target rock reflect the processes that ultimately led to vast biotic extinctions across the K–Pg boundary.

Conclusions

Following the K–Pg asteroid impact, organic carbon from sedimentary target rock was vaporized or pyrolyzed and ejected from what is now the Chicxulub crater as indicated by the distribution of PAHs. These compounds uniquely indicate rapidly heated carbon (indicated by isomer forms) that was derived from fossil sources (indicated by alkylation patterns) and was transported long distances by atmospheric processes (indicated by size distributions). PAHs deposited near the crater are dominated by larger and therefore less volatile and soluble structures, while smaller compounds were deposited at remote ocean sites. We infer that PAHs formed upon impact were emplaced in a dust cloud above the stratosphere (15, 16). Smaller PAHs in the dust cloud (15) remained as volatiles with extended atmospheric residence times before they were ultimately redeposited via sorption to dust particulate and precipitation (14, 51, 52). Charcoal and molecular evidence also indicate additional inputs from regional or global fires (26, 31), although fire inputs had a delayed effect on Earth's climate system. Our evidence indicates the target rock released a massive amount of climatically active carbon to Earth's upper atmosphere, where, along with sulfate aerosols and dust (16), it initiated the impact winter (14, 16, 48) that likely drove the end-Cretaceous mass extinction (9), making target-rock organic matter integral to extinction processes.

Our results support the previously hypothesized importance of crustal organic matter in the atmosphere on climate and extinction following the Chicxulub impact (14). Pyrolyzed organic matter and soot released to the upper atmosphere following the impact would have immediately blocked sunlight and contributed to the impact winter. Here, PAH evidence indicates smoke-like debris was retained in the upper atmosphere as a result of the Chicxulub impact. Thus, burn products from the impact site acted to intensify both the inhibition of photosynthesis and global cooling during the mass extinction, while wildfires had a delayed impact and increased the magnitude and duration of the impact winter.

Methods

Sediment samples obtained from sites M0077, 738, and 1262 were freeze-dried, and the outer layers of rock samples were removed with a solvent-cleaned blade prior to powdering by ball mill. Total lipid extracts were obtained via accelerated solvent extraction of ~12 g of sediment using 90% methylene chloride (DCM) and 10% methanol (MeOH) (vol/vol). Extracts

were dried to <1 mL under a stream of N_2. Lipid extracts were separated into fractions (aliphatic, aromatic, polar) using an accelerated solvent extraction method detailed in Magill et al. (2015) (85). Metal extraction cells were packed with layers of sand, diatomaceous earth, silver alumina, and silica gel stationary phases. The aliphatic fraction was eluted with 100% hexane; the aromatic fraction was eluted with 90% hexane and 10% DCM (vol/vol); the polar fraction was eluted with 70% DCM and 30% MeOH (vol/vol). All fractions were brought to close to dryness and redissolved in 50 μL of DCM. Aliphatic fractions were analyzed via gas chromatography–mass spectrometry (GC-MS) on a Thermo Scientific Trace 1310 gas chromatograph coupled to a Thermo Scientific ISQ LT single-quadrupole mass spectrometer. A Restek Rxi-5HT fused silica column (30-m length × 0.25-mm internal diameter × 0.25 μm) was used with a helium carrier gas. Oven program started with an injection temperature of 40 °C held for 1.5 min, followed by a rise of 15.0 °C/min until temperature reached 140 °C, after which temperature increased 6.0 °C/min until temperature reached 320 °C, at which the temperature was held for 20 min, for a total run time of 58 min. Ninety percent of flow was transferred to ISQ quadrupole mass spectrometer, transfer line temperature was 340 °C, and electron ionization was 300 °C, which scanned for a mass range of 50 to 550 *m/z* at 5 scans/s. Ten percent of the split flow was routed to a flame ionization detector (FID) held at 330 °C. Biomarker quantifications were determined from FID peak area, using AGSO standard oil, Macondo oil, and an *n*-C_{10} to *n*-C_{40} alkane standard and five-point calibration curve (Supelco). Mass spectra were used for compound identification by comparison with standards and published spectra. Aromatic fractions were run on a Hewlett-Packard 6890 gas chromatograph coupled to a Hewlett-Packard 5973 mass selective detector. The GC oven program started with an injection temperature of 40 °C held for 1 min, followed by a rise of 6.5 °C/min until temperature reached 320 °C. The injector and detector were held constant at 320 °C. Samples were injected in splitless mode onto a 30-m Rxi-XLB fused silica column (250 μm × 0.25 μm) via a Hewlett-Packard 7683 series autosampler. A portion of samples were run in full scan (mass range *m/z* 40 to 700) to identify alkylated PAHs, and all samples were quantified in selective ion monitoring mode using a five-point calibration curve of a 16 PAH standard suite (Sigma-Aldrich) and a separate retene standard suite (Sigma-Aldrich)

Data Availability. All data presented in this manuscript are made available as downloadable datasets in *SI Appendix*.

ACKNOWLEDGMENTS. This research used samples and data provided by the International Ocean Discovery Program (IODP). Expedition 364 was funded by the European Consortium for Ocean Research Drilling and the International Continental Scientific Drilling Program, with contributions from the Yucatán State Government and Universidad Nacional Autónoma de México. This study was funded by NSF-OCE 1737351, NSF-OCE 1736951, and Natural Environment Research Council Grant NE/P005217/1. We are grateful to D. Walizer, S. Lincoln, and H. Betz for analytical support. K.G. and B.S. thank the Australian Research Council (ARC) for an ARC-Discovery grant (DP180100982) entitled "The recovery of life recorded at the End-Cretaceous impact crater." B.S. thanks Curtin University for an Australian postgraduate award. A.T.K. was supported by a NSF Graduate Research Fellowship under Grant DGE1255832. This is University of Texas Institute for Geophysics Contribution #3685 and Center for Planetary Systems Habitability Contribution #0015. We thank the editor and two anonymous reviewers for their contributions to this manuscript.

1. N. Artemieva, J. Morgan, Expedition 364 science party, quantifying the release of climate-active gases by large meteorite impacts with a case study of Chicxulub. *Geophys. Res. Lett.* **44**, 10180–10188 (2017).
2. P. R. Renne *et al*., Time scales of critical events around the Cretaceous-Paleogene boundary. *Science* **339**, 684–687 (2013).
3. L. W. Alvarez, W. Alvarez, F. Asaro, H. V. Michel, Extraterrestrial cause for the Cretaceous-Tertiary extinction. *Science* **208**, 1095–1108 (1980).
4. G. S. Collins *et al*.; IODP-ICDP Expedition 364 Science Party; Third-Party Scientists, A steeply-inclined trajectory for the Chicxulub impact. *Nat. Commun.* **11**, 1480 (2020).
5. A. R. Hildebrand *et al*., Chicxulub crater: A possible Cretaceous/Tertiary boundary impact crater on the Yucatán Peninsula, Mexico. *Geology* **19**, 867–871 (1991).
6. G. S. Collins *et al*., Dynamic modeling suggests terrace zone asymmetry in the Chicxulub crater is caused by target heterogeneity. *Earth Plant. Sci. Lett.* **270**, 221–230 (2008).
7. J. V. Morgan *et al*., The formation of peak rings in large impact craters. *Science* **354**, 878–882 (2016).
8. D. Jablonski, D. M. Raup, Selectivity of end-Cretaceous marine bivalve extinctions. *Science* **268**, 389–391 (1995).
9. P. Schulte *et al*., The Chicxulub asteroid impact and mass extinction at the Cretaceous-Paleogene boundary. *Science* **327**, 1214–1218 (2010).
10. J. Brugger, G. Feulner, S. Petri, Baby, it's cold outside: Climate model simulations of the effects of the asteroid impact at the end of the Cretaceous. *Geophys. Res. Lett.* **44**, 419–427 (2017).
11. D. A. Kring, The Chicxulub impact event and its environmental consequences at the Cretaceous–Tertiary boundary. *Palaeogeogr. Palaeoclimatol. Palaeoecol.* **255**, 4–21 (2007).
12. O. B. Toon, R. P. Turco, C. Covey, Environmental perturbations caused by the impacts of asteroids and comets. *Rev. Geophys.* **35**, 41–78 (1997).
13. A. Chiarenza *et al*., Asteroid impact, not volcanism, caused the end-Cretaceous dinosaur extinction. *Proc. Natl. Acad. Sci. U.S.A.* **117**, 17084–17093 (2020).
14. K. Kaiho *et al*., Global climate change driven by soot at the K-Pg boundary as the cause of the mass extinction. *Sci. Rep.* **6**, 28427 (2016).
15. N. Artemieva, J. Morgan, Global K-Pg layer deposited from a dust cloud. *Geophys. Res. Lett.* **47**, e2019GL086562 (2020).
16. C. R. Tabor, G. G. Bardeen, B. L. Otto-Bliesner, R. R. Garcia, O. B. Toon, Causes and climatic consequences of the impact winter at the Cretaceous-Paleogene boundary. *Geophys. Res. Lett.* **47**, e60121 (2020).
17. F. T. Kyte, J. A. Bostwick, Magnesioferrite spinel in Cretaceous/Tertiary boundary sediments of the Pacific basin: Remnants of hot, early ejecta from the Chicxulub impact? *Earth Planet. Sci. Lett.* **132**, 113–127 (1995).
18. W. S. Wolbach, I. Gilmour, E. Anders, C. J. Orth, R. R. Brooks, Global fire at the Cretaceous-Tertiary boundary. *Nature* **334**, 665–669 (1988).
19. M. C. Harvey, S. C. Brassell, C. M. Belcher, A. Montanari, Combustion of fossil organic matter at the Cretaceous-Paleogene (K-P) boundary. *Geology* **36**, 355–358 (2008).
20. T. Arinobu, R. Ishiwatari, K. Kaiho, M. A. Lamolda, Spike of pyrosynthetic polycyclic aromatic hydrocarbons associated with an abrupt decrease in $\delta^{13}C$ of a terrestrial biomarker at the Cretaceous-Tertiary boundary at Caravaca, Spain. *Geology* **27**, 723–726 (1999).
21. M. A. Kruge, B. A. Stankiewicz, J. C. Crelling, A. Montanari, D. F. Bensley, Fossil charcoal in Cretaceous-Tertiary boundary strata: Evidence for catastrophic firestorm and megawave. *Geochim. Cosmochim. Acta* **58**, 1393–1397 (1994).
22. M. I. Venkatesan, J. Dahl, Organic geochemical evidence for global fires at the Cretaceous/Tertiary boundary. *Nature* **338**, 57–60 (1989).
23. W. S. Wolbach, R. S. Lewis, E. Anders, Cretaceous extinctions: Evidence for wildfires and search for meteoritic material. *Science* **230**, 167–170 (1985).
24. W. S. Wolbach, I. Gilmour, E. Anders, "Major wildfires at the Cretaceous/Tertiary boundary" in *Global Catastrophes in Earth History: An Interdisciplinary Conference on Impacts, Volcanism, and Mass Mortality*, V. L. Sharpton, P. D. Ward, Eds. (Geological Society of America, 1990), pp. 263–270.
25. T. J. Goldin, H. J. Melosh, Self-shielding of thermal radiation by Chicxulub impact ejecta: Firestorm or fizzle? *Geology* **37**, 1135–1138 (2009).
26. S. P. S. Gulick *et al*.; Expedition 364 Scientists, The first day of the Cenozoic. *Proc. Natl. Acad. Sci. U.S.A.* **116**, 19342–19351 (2019).
27. S. Pal, J. P. Shrivastava, S. K. Mukhopadhyay, Polycyclic aromatic hydrocarbon compound excursions and K/Pg transition in the late Cretaceous-early Palaeogene succession of the Um Sohryngkew river section, Meghalaya. *Curr. Sci.* **109**, 1140–1150 (2015).
28. H. Mita, A. Shimoyama, Distribution of polycyclic aromatic hydrocarbons in the K/T boundary sediments at Kawaruppu, Hokkaido, Japan. *Geochem. J.* **33**, 305–315 (1999).
29. C. M. Belcher, Reigniting the Cretaceous-Palaeogene firestorm debate. *Geology* **37**, 1147–1148 (2009).
30. B. R. T. Simoneit, H. R. Beller, "Lipid geochemistry of Cretaceous/Tertiary boundary sediments, Hole 605, Deep Sea Drilling Project Leg 93, and Stevns Klint, Denmark" in *Initial Reports of the Deep Sea Drilling Project*, J. E. van Hinte, Ed. *et al*. (US Government Printing Office, Washington, DC, 1987), Vol. 93, pp. 1211–1221.
31. T. J. Bralower *et al*., Origin of a global micrite layer in the aftermath of the Cretaceous-Paleogene boundary impact. *Earth Planet. Sci. Lett.* in press.
32. I. Gilmour, W. S. Wolbach, E. Anders, "Major wildfires at the Cretaceous-Tertiary boundary" in *Catastrophes and Evolution: Astronomical Foundations*, S. V. M. Clube, Ed. (Cambridge University Press, 1990), pp. 195–213.
33. I. Gilmour, M. A. Stephton, J. V. Morgan, "Organic geochemistry of a hydrocarbon-rich calcarenite from the Chicxulub Scientific Drilling Program" in *34th Lunar and Planetary Science Conference* (Lunar and Planetary Institute, 2003), no. 1771.
34. D. Heymann *et al*., Geochemical markers of the Cretaceous-Tertiary boundary event at Brazos River, Texas, USA. *Geochim. Cosmochim. Acta* **62**, 173–181 (1998).
35. W. S. Wolbach, "Carbon across the Cretaceous-Tertiary boundary," PhD dissertation, Department of Chemistry, University of Chicago, Chicago (1990).
36. W. S. Wolbach, S. Widicus, F. T. Kyte, A search for soot from global wildfires in central Pacific Cretaceous-Tertiary boundary and other extinction and impact horizon sediments. *Astrobiology* **3**, 91–97 (2003).
37. C. M. Belcher, M. E. Collinson, A. R. Sweet, A. R. Hildebrand, A. C. Scott, Fireball passes and nothing burns—the role of thermal radiation in the Cretaceous-Tertiary event: Evidence from the charcoal record of North America. *Geology* **31**, 1061–1064 (2003).
38. D. Heymann, L. P. F. Chibante, R. R. Brooks, W. S. Wolbach, R. E. Smalley, Fullerenes in the Cretaceous-Tertiary boundary layer. *Science* **265**, 645–647 (1994).
39. L. C. Ivany, R. J. Salawitch, Carbon isotopic evidence for biomass burning at the K-T boundary. *Geology* **21**, 487–490 (1993).
40. D. S. Robertson, W. M. Lewis, P. M. Sheehan, O. B. Toon, K-Pg extinction: Reevaluation of the heat-fire hypothesis. *JGR Biogeosci.* **118**, 329–336 (2013).
41. J. Morgan, N. Artemieva, T. Goldin, Revisiting wildfires at the K-Pg boundary. *J. Geophys. Res. Biogeosci.* **118**, 1508–1520 (2013).

42. H. J. Melosh, N. M. Schneider, K. J. Zahnle, D. Latham, Ignition of global wildfires at the Cretaceous/Tertiary boundary. *Nature* **343**, 251–254 (1990).
43. E. Stogiannidis, R. Laane, Source characterization of polycyclic aromatic hydrocarbons by using their molecular indices: An overview of possibilities. *Rev. Environ. Contam. Toxicol.* **234**, 49–133 (2015).
44. K. Grice *et al*., New insights into the origin of perylene in geological samples. *Geochim. Cosmochim. Acta* **73**, 6531–6543 (2009).
45. A. I. Holman, K. Grice, C. M. B. Jaraula, A. Schimmelmann, Bitumen II from the Paleoproterozoic Here's Your Chance Pb/Zn/Ag deposit: Implications for the analysis of depositional environment and thermal maturity of hydrothermally-altered sediments. *Geochim. Cosmochim. Acta* **139**, 98–109 (2014).
46. K. H. Williford, K. Grice, G. A. Logan, J. Chen, D. Huston, The molecular and isotopic effects of hydrothermal alteration of organic matter in the Paleoproterozoic McArthur river Pb/Zn/Ag ore deposit. *Earth Planet. Sci. Lett.* **301**, 382–392 (2011).
47. B. R. T. Simoneit, P. F. Lonsdale, Hydrothermal petroleum in mineralized mounds at the seabed of Guaymas Basin. *Nature* **295**, 198–202 (1982).
48. C. G. Bardeen, R. R. Garcia, O. B. Toon, A. J. Conley, On transient climate change at the Cretaceous-Paleogene boundary due to atmospheric soot injections. *Proc. Natl. Acad. Sci. U.S.A.* **114**, E7415–E7424 (2017).
49. T. Kenkmann, A. Wittmann, D. Scherler, Structure and impact indicators of the Cretaceous sequence of the ICDP drill core Yaxcopoil-1, Chicxulub impact crater, Mexico. *Meteorit. Planet. Sci.* **39**, 1069–1088 (2004).
50. C. M. Belcher, M. E. Collinson, A. C. Scott, Constraints on the thermal energy released from the Chicxulub impactor: New evidence from multi-method charcoal analysis. *J. Geol. Soc. London* **162**, 591–602 (2005).
51. P. Yu *et al*., Black carbon lofts wildfire smoke high into the stratosphere to form a persistent plume. *Science* **365**, 587–590 (2019).
52. T. C. Bond *et al*., Bounding the role of black carbon in the climate system: A scientific assessment. *J. Geophys. Res. Atmos.* **118**, 5380–5552 (2013).
53. V. V. Shuvalov, N. A. Artemieva, Numerical modeling of Tunguska-like impacts. *Planet. Space Sci.* **50**, 181–192 (2002).
54. C. M. Belcher *et al*., An experimental assessment of the ignition of forest fuels by the thermal pulse generated by the Cretaceous–Palaeogene impact at Chicxulub. *J. Geol. Soc. London* **172**, 175–185 (2015).
55. N. Oshima *et al*., Wet removal of black carbon in Asian outflow: Aerosol radiative forcing in East Asia (A-FORCE) aircraft campaign. *J. Geophys. Res. Atmos.* **117**, D03204 (2012).
56. C. M. Lowery *et al*., Rapid recovery of life at ground zero of the end-Cretaceous mass extinction. *Nature* **558**, 288–291 (2018).
57. S. Goderis, "The final settling of meteoritic matter on the peak-ring of the Chicxulub impact structure in Core M0077A of IODP-ICDP expedition 364" in *Large Meteorite Impacts and Planetary Evolution VI*, (Lunar and Planetary Institute, 2019), pp. 13–14.
58. G. Bohrmann, W. U. Ehrmann, "Analysis of sedimentary facies using bulk mineralogical characteristics of Cretaceous to quaternary sediments from the Kerguelen Plateau: Sites 737, 738, and 744" in *Proceedings of the Ocean Drilling Program, Scientific Results, Volume 119*, J. Baron, B. Larson, Eds. (Ocean Drilling Program, Texas A&M University, 1991), pp. 211–223.
59. B. Schmitz, F. Asaro, H. V. Michel, H. R. Thierstein, B. T. Huber, "Element stratigraphy across the Cretaceous/Tertiary boundaiy in Hole 738C" in *Proceedings of the Ocean Drilling Program, Scientific Results, Volume 119*, J. Baron, B. Larson, Eds. (Ocean Drilling Program, Texas A&M University, 1991), pp. 719–730.
60. J. C. Zachos, D. Kroon, P. Blum, Site 1262. *Proc. Ocean Drill. Program, Initial Rep.* **208**, 1–92 (2004).
61. J. S. K. Barnet *et al*., A high-fidelity benthic stable isotope record of late Cretaceous–Early eocene climate change and carbon-cycling. *Paleoceanogr. Paleoclimatol.* **34**, 672–691 (2019).
62. G. Bernaola, S. Monechi, Calcareous nannofossil extinction and survivorship across the Cretaceous-Paleogene boundary at Walvis Ridge (ODP Hole 1262C, South Atlantic Ocean). *Palaeogeogr. Palaeoclimatol. Palaeoecol.* **255**, 132–156 (2007).
63. G. Ravizza, D. Vonderhaar, A geochemical clock in earliest Paleogene pelagic carbonates based on the impact-induced Os isotope excursion at the Cretaceous-Paleogene boundary. *Paleoceanography* **27**, 1–15 (2012).
64. T. J. Bralower *et al*., The habitat of the nascent Chicxulub crater. *AGU Advances.* in press.
65. H. R. Thierstein *et al*., The Cretaceous/Tertiary boundary at site 738, southern Kerguelen Plateau. *Proc. Ocean Drill. Program Sci. Results* **119**, 849–867 (1991).
66. P. M. Hull, P. J. S. Franks, R. D. Norris, Mechanisms and models of iridium anomaly shape across the Cretaceous-Paleogene boundary. *Earth Planet. Sci. Lett.* **301**, 98–106 (2011).
67. A. T. Karp, A. I. Holman, P. Hopper, K. Grice, K. H. Freeman, Fire Distinguishers: Refined interpretations of paleofire from polycyclic aromatic hydrocarbons. *Geochim. Cosmochim. Acta* **289**, 93–113 (2020).
68. Z. Wang *et al*., Quantitative characterization of PAHs in burn residue and soot samples and differentiation of pyrogenic PAH1 from petrogenic PAHs—the 1994 mobile burn study. *Environ. Sci. Technol.* **33**, 3100–3109 (1999).
69. S. A. Stout, J. R. Payne, Chemical composition of floating and sunken in-situ burn residues from the Deepwater Horizon oil spill. *Mar. Pollut. Bull.* **108**, 186–202 (2016).
70. R. Wang, P. Cadman, Soot and PAH production from spray combustion with different hydrocarbons behind reflected shock waves. *Combust. Flame* **112**, 359–370 (1998).
71. A. C. Rocha, C. Palma, Source identification of polycyclic aromatic hydrocarbons in soil sediments: Application of different methods. *Sci. Total Environ.* **652**, 1077–1089 (2019).
72. M. Tobiszewski, J. Namieśnik, PAH diagnostic ratios for the identification of pollution emission sources. *Environ. Pollut.* **162**, 110–119 (2012).
73. M. B. Yunker *et al*., PAHs in the Fraser River basin: A critical appraisal of PAH ratios as indicators of PAH source and composition. *Org. Geochem.* **33**, 489–515 (2002).
74. H. Budzinski *et al*., Alkylated phenanthrene distributions as maturity and origin indicators in crude oils and rock extracts. *Geochim. Cosmochim. Acta* **59**, 2043–2056 (1995).
75. O. Botta *et al*., Polycyclic aromatic hydrocarbons and amino acids in meteorites and ice samples from LaPaz Icefield, Antarctica. *Meteorit. Planet. Sci.* **43**, 1465–1480 (2008).
76. L. Becker, D. P. Glavin, J. L. Bada, Polycyclic aromatic hydrocarbons (PAHs) in Antarctic Martian meteorites, carbonaceous chondrites, and polar ice. *Geochim. Cosmochim. Acta.* **61**, 475–481 (1997).
77. P. D. Boehm *et al*., Distribution and weathering of crude oil residues on shorelines 18 years after the Exxon Valdez spill. *Environ. Sci. Technol.* **42**, 9210–9216 (2008).
78. T. Salge, H. Stosnach, G. Rosatelli, L. Hecht, W. U. Reimold, Evidence for shock-induced anhydrite recrystallization and decomposition at the UNAM-7 drill core from the Chicxulub impact structure. *Meteorit. Planet. Sci.* **2356**, 2334–2356 (2019).
79. B. Schaefer *et al*., Microbial life in the nascent Chicxulub crater. *Geology* **48**, 328–332 (2020).
80. N. Artemieva, J. Morgan, Modeling the formation of the K-Pg boundary layer. *Icarus* **201**, 768–780 (2009).
81. E. Pierazzo, D. A. Kring, H. J. Melosh, Hydrocode simulation of the Chicxulub impact event and the production of climatically active gases. *J. Geophys. Res.* **103**, 28607–28625 (1998).
82. V. Lüders, T. Horsfeld, T. Kenkmann, B. Mingram, A. Wittmann, "Hydrocarbon and aqueous fluids in Cretaceous sediments of the ICDP-Chicxulub drill core Yax-1" in *34th Lunar and Planetary Science Conference* (Lunar and Planetary Institute, 2003), no. 1378.
83. E. López-Ramos, "Geological summary of the Yucatán Peninsula" in *The Ocean Basins and Margins Volume 3*, F. G. Stehli, A. E. Nairn, Eds. (Plenum Press, ed. 3, 1975), pp. 257–282.
84. R. P. Turco, O. B. Toon, T. P. Ackerman, J. B. Pollack, C. Sagan, Climate and smoke: An appraisal of nuclear winter. *Science* **247**, 166–176 (1990).
85. C. R. Magill, E. H. Denis, K. H. Freeman, Rapid sequential separation of sedimentary lipid biomarkers via selective accelerated solvent extraction. *Org. Geochem.* **88**, 29–34 (2015).